Journal of Colloid and Interface Science 559 (2020) 51–64

Contents lists available at ScienceDirect

Journal of Colloid and Interface Science

journal homepage: www.elsevier.com/locate/jcis

Triple stimuli-responsive ZnO quantum dots-conjugated hollow mesoporous carbon nanoplatform for NIR-induced dual model antitumor therapy

Shuang Feng [a], Yuling Mao [a], Xiudan Wang [a], Meiting Zhou [b], Hongyan Lu [a], Qinfu Zhao [a,*], Siling Wang [a,*]

[a] Department of Pharmaceutics, School of Pharmacy, Shenyang Pharmaceutical University, 103 Wenhua Road, Shenyang, Liaoning Province 110016, PR China
[b] Department of Inorganic Chemistry, School of Pharmaceutical Engineering, Shenyang Pharmaceutical University, 103 Wenhua Road, Shenyang, Liaoning Province 110016, PR China

GRAPHICAL ABSTRACT

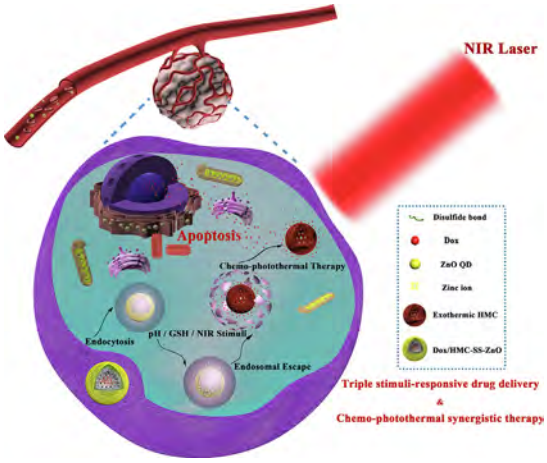

ARTICLE INFO

Article history:
Received 23 July 2019
Revised 27 September 2019
Accepted 28 September 2019
Available online 30 September 2019

Keywords:
Hollow mesoporous carbon nanoparticles
ZnO quantum dots
TEM-EDX mapping
Triple stimuli-responsive
Chemo-photothermal synergistic therapy

ABSTRACT

Aiming at the inefficiency and toxicity in traditional antitumor therapy, a novel multifunctional nanoplatform was constructed based on hollow mesoporous carbon (HMC) to achieve triple stimuli response and dual model antitumor therapy *via* chemo-photothermal synergistic effect. HMC was used as an ideal nanovehicle with a high drug loading efficiency as well as a near-infrared (NIR) photothermal conversion agent for photothermal therapy. Acid-dissoluble, luminescent ZnO quantum dots (QDs) were used as the proper sealing agents for the mesopores of HMC, conjugated to HMC *via* disulfide linkage to prevent drug (doxorubicin, abbreviated as Dox) premature release from Dox/HMC-SS-ZnO. After cellular endocytosis, the Dox was released in a pH, GSH and NIR laser triple stimuli-responsive manner to realize accurate drug delivery. Moreover, the local hyperthermia effect induced by NIR irradiation could promote the drug release, enhance cell sensitivity to chemotherapeutic agents, and also directly kill cancer cells. As expected, Dox/HMC-SS-ZnO exhibited a high drug loading capacity of 43%, well response to triple stimuli and excellent photothermal conversion efficiency η of 29.7%. The therapeutic efficacy in 4T1 cells and multicellular tumor spheroids (MCTSs) demonstrated that Dox/HMC-SS-ZnO + NIR had satisfactory chemo-photothermal synergistic effect with a combination index (CI) of 0.532. The cell apoptosis rate

* Corresponding authors.
E-mail addresses: qinfuzhao@syphu.edu.cn (Q. Zhao), silingwang@syphu.edu.cn (S. Wang).

https://doi.org/10.1016/j.jcis.2019.09.120

of the combined treatment group was more than 95%. The biodistribution and pharmacodynamics studies showed its biosecurity to normal tissues and synergistic inhibition effect to tumor cells. These distinguished results indicated that the Dox/HMC-SS-ZnO nanoplatform is potential to realize efficient triple stimuli-responsive drug delivery and dual model chemo-photothermal synergistic antitumor therapy.

1. Introduction

Despite the optimistic developing of numerous scientific researches to tackle the cancer problem, a tremendous challenge is still remaining due to the complexities and variabilities involved in tumorigenesis and progression. Chemotherapy is one of the most general therapeutic method in the clinic application with great progress in tumor proliferation suppression and life prolonging of patients. However, conventional chemotherapy drugs are often limited by the lacking of specificity and selectivity for the tumor sites, which could lead to the systemic toxicity and serious adverse effects [1,2]. Nanocarrier-mediated stimuli-responsive drug delivery system has aroused widely concern recently owing to the great merits of precise delivery of drugs through convenient switching effect for controlled drug release by specific stimulations [3,4]. Thus, plentiful stimuli-responsive drug delivery systems which are sensitive to physicochemical stimuli (e.g., temperature, redox, and pH) [5,6], or biochemical stimuli (e.g., enzymes, cytokines, and glucose) [7–9] have been developed to improve antitumor efficiency.

Moreover, another application hinder of chemotherapy alone is the multidrug-resistance (MDR) mainly resulted from acceleration of anticancer drug efflux mediated by the P glycoprotein membrane transporters [10–13]. As a promising alternative to conventional antitumor therapeutic approaches, the near-infrared (NIR) laser-induced multi-model combination therapeutic approaches have aroused noticeable focus because of its maximally efficient and minimally invasive treatment outcome [14–17]. The NIR laser within 700–1100 nm wavelength is the transparent ‘‘therapeutic window” for clinical applications owing to its deeper tissue penetration capacity and comparatively less damage to healthy tissue. Wu et al. successfully developed a magnetic hollow porous carbon nanoparticles (MHPCNs) to overcome MDR produced by chemotherapy through utilizing photothermal conversion property of carbon and iron oxide (Fe_3O_4) nanomaterials to perform NIR-induced photothermal therapy (PTT) [18]. Cheng et al. fabricated a novel nanocluster probe (Ag_2S/chlorin e6 (Ce6)/DOX@DSPE-mPEG2000-folate) with multifunction including fluorescence, and photoacoustic dual-mode imaging, and excellent photothermal, photodynamic (PDT) and chemotherapeutic antitumor effects [19]. In the antitumor therapy study, this nanoplatform with NIR irradiation exhibited efficient multi-model therapeutic effects on tumors. Similarly, several other interesting studies have been performed by using various NIR absorbing nanoparticles (e.g., Au NRs and nano-MOFs) as photosensitizer (e.g., ICG and Ce6) and chemotherapeutic drugs delivery carriers to achieve combination therapy [20,21]. In particular, cancer PTT mediated by nanomaterials for multi-model antitumor therapy has attracted much attention of researchers worldwide. Under NIR irradiation, NIR resonant materials can rapidly generate local hyperthermia to cause cell damage and minimize injury to surrounding normal cells [22,23]. Besides, hyperthermia induced by PTT can also promote the cellular uptake, trigger drug release and result in antitumor efficacy enhancement. Therefore, the ideal nanoplatform-based drug delivery systems (DDSs) should integrate precise drug delivery and synergistic PTT capacity to achieve effect-enhancing and toxicity-reducing win-win effect in cancer therapy.

A great number of photothermal nanomaterials have been gradually developed in recent years [24,25]. Organic photothermal nanomaterials are widely used for nanobiotechnology owing to excellent biocompatibility [26–28]. However, the poor photothermal conversion capacity and photothermal stability extremely limit their application for PTT. By contrast, inorganic photothermal materials owning extraordinary photothermal conversion efficiency and the good thermostability may be expected to meet the requirements for synergistic PPT. Among these inorganic NIR absorbing nanomaterials, carbon-based nanoparticles with forceful π–π conjugated structures have drawn great attention owing to their drug delivery ability and biosecurity. Compare with the carbon nanotubes (CNT) and two-dimensional graphene [29–33], three-dimensional mesoporous carbon nanoparticles are highly prospective for the antitumor treatment resorting to their superior merits including huge specific surface area and pore volume, proper particle size, tunable surface properties and good biocompatibility [34–38]. Even more encouragingly, MCN with outstanding photothermal characteristics could effectively transform the absorbed NIR laser into heat energy for chemo-photothermal synergistic therapy [39]. Inspired by these outstanding features, hollow mesoporous carbon (HMC) nanoparticles possess many unique advantages, such as large hollow cavities to improve drug loading capacity, easily functionalized surface for multifunction modification, as well as more excellent photothermal conversion efficiency due to the typical hollow structure. Herein HMC could be used to establish a chemo-photothermal therapeutic nanoplatform that respond to the stimuli in the heterogeneous cells to control drug release and overcome the therapeutic barriers mentioned above.

The regulation of drug release by heterogeneous cells provides important theoretical basis for the design of intelligent nanoplatforms. Glutathione (GSH), the abundant thiol-containing peptide involved in many important functions in animals, is found with high intracellular concentrations (0.5–10 mM) and very low extracellular concentrations (<10 μM). Moreover, about 4 times higher concentrations of GSH in the tumor tissues than the normal tissues, that rendered the redox-sensitive nanoparticles available for tumor-specific drug delivery [40–45]. Redox-sensitive disulfide bonds remain stable in the circulation system, while they are ruptured immediately to promote drug release under the high-concentration GSH in the tumor cells [46,47]. Additionally, pH value is another representative stimulus [48,49]. The pH in tumor microenvironment (~pH 6.0) is much more acidic than in body fluid, especially further declines in the early endosomes and late endosomes/lysosomes of the cancer cells with the approximate pH of 5.5 and 5.0, respectively. So far, through reasonable design, we anticipate that such HMC-based drug delivery system could realize a satisfactory drug loading efficiency, simultaneously to be tumor specific, intracellular stimuli sensitive, drug release controlled and capable of photothermal conversion upon NIR irradiation. For the HMC-based drug delivery system, appropriate gatekeepers are necessary and crucial to block the pore entrances to achieve controlled drug release and prevent premature leakage in circulation system. To date, diverse gatekeepers including macromolecular polymers [50,51], inorganic nanoparticle [52], biomacromolecules [53,54], and quantum dots (QDs) [55,56] have

been developed depending on different stimuli requirements. In last decades, ZnO quantum dots have been widely applied for the bio-imaging owing to their outstanding luminescent properties, biocompatibility and high thermal stability. And their other desirable traits were discovered recently such as their ability to produce destructive reactive oxygen species (ROS), release Zn^{2+} ions in acidic media and their versatile surface chemistry, making them promising potential for the treatment of cancer, anti-microbes and diabetes [57,58]. ZnO QDs may be satisfactory pH sensitive gatekeepers, because they are pretty stable at pH 7.4 environment but immediately dissolved into Zn^{2+} upon pH below 5.5 [59]. Once the nanocarriers are taken into cancer cells by endocytosis, the acidic media will promote hydrolysis of ZnO QDs and trigger efficient drug release.

Herein, we rationally constructed a novel pH-, redox- and NIR-triple stimuli-responsive HMC nanoplatform (HMC-SS-ZnO) for chemo-photothermal synergistic therapy for cancer disease (Scheme 1). Doxorubixin (Dox), a chemotherapeutic drug with broad therapeutic range, was selected as a model drug. HMC-based nanoplatforms (Dox/HMC-SS-ZnO) not merely acted as a large reservoir for improving the drug-loading capacity, but also were used as the NIR resonant materials to convert NIR light into thermal effect for tumor ablation. Upon cellular uptake of Dox/HMC-SS-ZnO into endo-lysosomes through endocytosis after the enhanced permeation and retention (EPR)-mediated targeting to tumor, ZnO QDs gatekeepers were rapidly hydrolyzed in the acid environment and the disulfide bonds were simultaneously quickly broken under the high concentration of GSH realizing drug release, furthermore, a promotive drug escape from the endosomes to nuclei could be triggered by NIR irradiation. The physicochemical characteristics, triple stimuli-responsive drug release manner, and thermal heating capacity were well investigated. The synergistic effects of antitumor therapy and cell death mechanisms of both HMC-mediated photothermal ablation and cytotoxicity of NIR-triggered drug release were studied. Then, the chemo-photothermal synergistic therapeutic effect in xenografted tumor animal model were explored. These results showed that systemic toxicity of Dox could be minimized and antitumor effect was greatly enhanced. The versatile Dox/HMC-SS-ZnO nanoparticles which clustered all the functional elements in one could realize a satisfying drug loading efficiency, tumor specific, intracellular stimuli-sensitive, drug release controlled and chemo-photothermal synergistic therapy, which may be an encouraging nanoplatform for drug delivery and a dual-model therapy for tumor disease.

2. Materials & methods

2.1. Chemical reagents

1-ethyl-3-(3-dimethylaminopropyl) carbodiimide hydrochloride (EDC) and N-hydroxysuccinimide (NHS), 3-Aminopropyltrimethoxysilane (APTMS), tetraethoxysilane (TEOS), cetyltrimethylammonium bromide (CTAB) and zinc acetate were

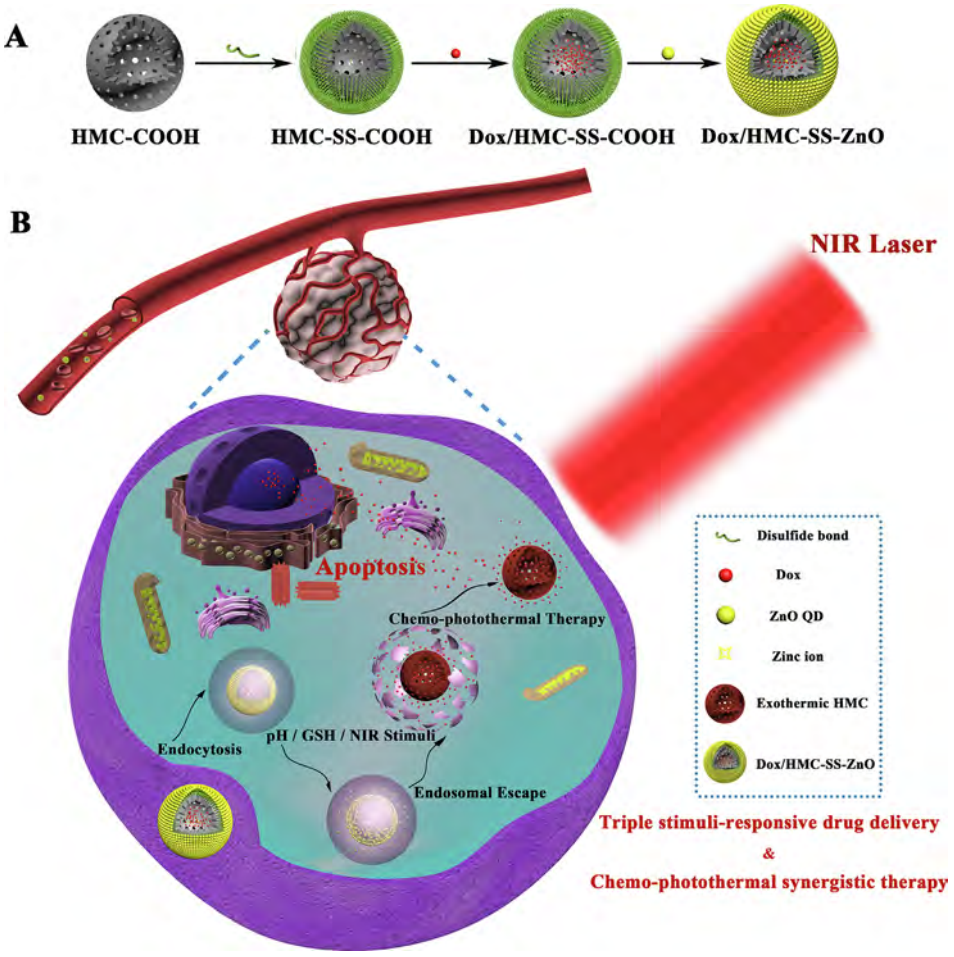

Scheme 1. (A) Construction procedures of Dox/HMC-SS-ZnO drug delivery nanoplatform; (B) Schematic illustration of the triple stimuli-responsive and dual-model antitumor effect with chemo-photothermal synergistic therapy.

ordered from Aladdin reagent Shanghai Com. Ltd. Penicillin-streptomycin and trypsin-EDTA solution (0.25%) were all supplied by GIBCO, Invitrogen Com. (Carlsbad, USA). Roswell Park Memorial Institute (RPMI)-1640, fluorescent dyes, 3-(4,5-Dimethylthiazol-2-yl)-2,5-diphenyltetrazolium bromide (MTT), and Annexin V-FITC/PI apoptosis detection kits were all bought from Dalian Meilune Biotech Com. Ltd. (Dalian, China). All chemical reagents were analytical grade and used without any further purification.

2.2. Instruments

The morphological feature was acquired by transmission electron microscopy (TEM, Tecnai G2F30; FEI; Eindhoven, Netherlands). The crystalline structure was measured by X-ray diffraction (XRD, Rigaku Geigerflex X-ray diffractometer, Japan) and differential scanning calorimeter (DSC, Mettler-Toledo, Switzerland). The optical properties were investigated by Fourier transfer infrared (FT-IR) spectra on Bruker IFS (Switzerland). The surface area and pore size distribution were determined from N_2 adsorption/desorption isotherms collected by V-Sorb 2800P (Gold APP Instrument Corporation, Beijing, China). The size distribution and mean diameter was measured by using Particle Size Analyzer Nicomp 380 (Particle Sizing Systems, USA). X-ray photoelectron spectroscopy (XPS) data and cellular imaging were performed by X-ray photoelectron spectrometer (ESCALAB 250Xi spectrometer, Thermo Fisher Scientific, USA) and confocal laser scanning microscope (CLSM, Zeiss LSM 510), respectively.

2.3. Preparation of ZnO QDs and APTMS modification

880 mg, 4 mmol $ZnAc_2{\cdot}2H_2O$ and 88 mg, 0.4 mmol $MgAc_2{\cdot}4H_2O$ were refluxed in 60 mL ethanol at 80 °C for 2 h. 20 mL NaOH (2.5 mM in anhydrous ethanol) was added rapidly to the mixture and refluxed for 6 h with continuous stirring. ZnO QDs were precipitated with excessive hexane, and calculated the quantum yield of ZnO QDs (details in supporting information S1).

Precipitated ZnO QDs (200 mg) were dispersed uniformly in N, N-dimethylformamide (DMF, 20 mL). 100 μL APTMS was added to the above dispersion solution with continuous stirring at 120 °C for 20 min. After centrifugation, the NH_2-ZnO QDs were dispersed in deionized water for standby.

2.4. Preparation of HMC and multifunctional modification

HMC and S-(2-Aminoethylthio)-2-thiopyridine hydrochloride (Py-SS-NH_2) were synthesized according to the literature reported previously [60]. The carboxylated HMC (HMC-COOH) were prepared *via* wet oxidation method using ammonium persulfate solution and H_2SO_4 mixture with refluxing at 60 °C for 3 h. 100 mg HMC-COOH were well dispersed in 30 mL pH 7.4 phosphate buffer solution (PBS) with NHS and EDC for carboxyl activation following by reacting with 75 mg Py-SS-NH_2 for 12 h to obtain HMC-SS-Py. After centrifugation, 3-mercaptopropionic acid (40 μL) was dropped into HMC-SS-Py ethanol suspension (4 mg mL^{-1}) with stirring for 24 h to attain HMC-SS-COOH.

2.5. Synthesis of Dox/HMC-SS-ZnO and in vitro drug release

10 mg Dox and 10 mg HMC-SS-COOH nanoparticles were dispersed in 2 mL PBS (pH 7.4) and stirred overnight. Obtained Dox/HMC-SS-COOH were mixed with carboxyl activation reagents NHS and EDC for 1 h, following by capping with NH_2-ZnO QDs 500 μL mentioned above for 24 h, then washing with PBS (pH 7.4) until the supernatant being clear to obtain Dox/HMC-SS-ZnO. Total washing liquids were collected to calculate the drug loading efficiency.

The drug release profiles *in vitro* were investigated in different release media. The Dox-loaded HMC with or without ZnO QDs-gated were dispersed in 5 mL of PBS (pH 7.4 or 5.0 with or without 10 mM GSH) and placed in 37 °C shaking bed. 1 mL release solution of each group was taken out to measure the Dox concentration at each predefined time interval. The amount of released drug was measured at 480 nm by ultraviolet–visible spectrophotometry (UV–Vis spectrophotometry). For the NIR-triggered release groups, the samples were irradiated under 808 nm NIR laser (1.0 W cm^{-2}) for 3 min at designed time intervals prior to measurement.

2.6. Dispersion stability and photothermal heating efficiency

10 mg HMC-COOH and HMC-SS-ZnO were well dispersed in 5 mL water and PBS (pH 7.4), respectively. At specified time points, the dispersion stabilities of samples were evaluated by determining the particle sizes and polydispersity indexes (PDI). The photothermal heating stability of HMC-SS-ZnO was investigated *via* repeatedly irradiating with 808 nm NIR laser (1.0 W cm^{-2}) to a particular temperature, then cooling, and the heating data was recorded using a thermal imager. The detailed calculation method of the photothermal conversion efficiency are displayed in the supporting information S2. Furthermore, samples were irradiated under a fixed power density of 1.0 W cm^{-2} at different concentrations and different power densities at a fixed concentration of 50 μg mL^{-1}.

2.7. Hemocompatibility test

Red blood cells (RBCs) were obtained from rabbits' atria. After centrifugation and being diluted using normal saline, 1 mL of the diluted cell suspension was mixed with 1 mL of samples including HMC-COOH or HMC-SS-ZnO with different concentrations. After stilled standing for 4 h, the absorbance values of the supernatants were measured using UV–Vis spectrophotometer at 540 nm.

2.8. Cellular photothermal effects induced by NIR laser

4T1 cell line was used for *in vitro* biological experiments, which was incubated in RPMI-1640 medium with FBS and streptomycin-penicillin (10% and 1%, v/v) in cell-use six-well plates within an atmosphere of 5% CO_2 at 37 °C. After incubated 24 h, cells were treated with different concentrations of HMC-SS-ZnO and then incubated for 2 h. Routinely, after cell digestion, collection and resuspension, samples were irradiated by NIR laser of 1.0 W cm^{-2} for 3 min.

2.9. Live/Dead cell assay

For Live/Dead cell assay, 4T1 cells were seeded into 24-well plates at a density of 1×10^5 cells each well. After treatments with preset formulations for 2 h, cells were stained with Calcein-AM/PI according to the product descriptions and observed by CLSM.

2.10. Cellular uptake of Dox/HMC-SS-ZnO

The cellular uptake of Dox/HMC-SS-ZnO was evaluated *via* CLSM and flow cytometry technique (FCM). Briefly, 4T1 cells were incubated in 6-well routinely, and treated with sterilized free Dox and Dox/HMC-SS-ZnO (based on Dox dosing of 5 μg mL^{-1}). After 1, 2 and 4 h of incubation, Dox fluorescence was measured using FCM. Additionally, 4T1 cells were cultured into 24-well plates. After dosing treatments for 1, 2 and 4 h, the cells were stained with Hoechst 33258 and observed by CLSM.

2.11. In vitro cytotoxicity assay

For the cytotoxic assay, 4T1 cells were cultured into 96-well plates following by treatment of different formulations with concentration gradients for another 24 h incubation. Afterwards, subdivided each group into two subgroups: with/without NIR irradiation. The former was irradiated with 808 nm NIR laser for 3 min (1.0 W cm^{-2}). Finally, we determined cell viabilities using the MTT method. Calculation of the combination index (CI): CI = [$IC_{50\ (combined\ therapy)}/IC_{50\ (chemotherapy\ alone)}$] + [$IC_{50\ (combined\ therapy)}/IC_{50\ (PTT\ alone)}$]. The CI value < 1 indicates synergism, CI value >1 shows antagonism, and CI value = 1 means additive effects.

2.12. Cell apoptosis test

To investigate cell apoptosis and necrosis induced by PTT, chemotherapy, and synergistic therapy, respectively. 4T1 cells were seeded for one day in 6-well plates at a density of 5×10^5 cells each well. The formulations were administered according to different prescriptions. The NIR irradiation groups were irradiated with NIR laser of 1.0 W cm^{-2} for 3 min after dosing 2 h. Then, the cells in each group were collected and stained with Annexin V-FITC/PI for readily FCM analysis.

2.13. Therapeutic efficacy on multicellular tumor spheroids (MCTSs)

Monolayer cultured 4T1 cells were digested and prepared into single-cell suspension. The cells were inoculated into 96-well plates with agar at the density of 3000 cells each well with new culture solution changing every two days. After tumor spheroids forming, the formulation treatments were same as apoptosis test above. The growth condition of MCTSs was recorded by microscopy, and CLSM was employed to detect the fluorescence signal intensity of Calcein AM/PI staining.

2.14. In vivo antitumor effect by combination therapy

BALB/c mice (18–20 g) were used for tumor-bearing modelling with subcutaneous inoculation of 4T1 cells (1×10^7 cells) into the right flanks. After randomly grouping into six experimental groups (n = 5) with normal saline (control), normal saline + NIR, free Dox (10 mg kg^{-1}), HMC-SS-ZnO + NIR, Dox/HMC-SS-ZnO, and Dox/HMC-SS-ZnO + NIR, respectively. For NIR irradiation groups, local tumors of mice were irradiated by NIR laser at 1.0 W cm^{-2} for 5 min after dosing 6 h later. Body weights and tumor volumes of mice were monitored for 15 days. The major organs and tumors were collected when experiment ended, fixed with 4% paraformaldehyde and paraffin processed for pathological analysis by hematoxylin and eosin (H&E) staining.

2.15. In vivo biodistribution

The tumor-bearing mice were treated with free Dox and Dox/HMC-SS-ZnO ± NIR, respectively. 2, 6 and 12 h later, the main organs (heart, liver, spleen, lung, and kidney) and tumors were gathered, and the Dox fluorescence intensity was detected immediately by IVIS system at the 480 nm wavelength.

3. Results & discussions

3.1. Characterization of ZnO QDs and APTMS modified ZnO QDs

The morphology features of ZnO QDs were identified *via* TEM and atomic force microscope (AFM) techniques. As shown in Fig. 1A, B, the uniformly dispersed spherical ZnO QDs with a mean particle size of 4–6 nm were displayed in TEM. The AFM results showed that the average height of ZnO QDs was 5.21 nm which was consistent with TEM consequences. The crystalline structure of ZnO QDs were investigated by the XRD (Fig. 1F). 31.8°, 34.5° and 36.2° peaks were corresponding to the quartzite structure reflections (1 0 0), (0 0 2) and (1 0 1) of ZnO QDs, respectively. All characteristic peaks were basically consistent with the standard pattern of ZnO (JCPDS NO. 36-1451). Moreover, the UV–Vis absorption spectrum, fluorescence spectra and photoluminescence (PL) emission spectra were detected to study the optical properties of ZnO QDs, and the quantum yield of ZnO QDs was 7.2%. (Fig. 1C, D, and S1).

Subsequently, the well water-dispersible, luminescent ZnO QDs with APTMS surface modification were prepared. FT-IR provided the surface functional groups features of ZnO QDs (Fig. 1G). Compared to naked ZnO QDs, two strong peaks at 1050 cm^{-1} and 1580 cm^{-1} appeared in NH_2-ZnO QDs FT-IR spectrum reflected the Si-O-Si stretch vibration and N—H bend vibration, respectively, indicating successful grafting of APTMS to ZnO QDs. Furthermore, XPS analysis provided additional evidence about APTMS modification in Fig. 1H, and the specific data are displayed in Table S1. Compared to the naked ZnO QDs, the appearance of two new peaks of N 1s at 404 eV and Si 2p at 105 eV with the element proportions of 5.66% and 6.76% respectively, proved the amino modification of ZnO QDs.

Importantly, the acidic dissolution properties of the NH_2-ZnO QDs were investigated in PBS with different pH (4.0–8.0), followed by measuring the fluorescence intensity of NH_2-ZnO QDs after incubation for 2 h. Fig. 1E illustrated that as the acidity of the buffer solution increased, the fluorescence intensity of NH_2-ZnO QDs decreased, and completely disappeared when pH blew 5.0, confirming that ZnO QDs could be stable at physiological pH (about 7.4) but rapidly dissolved in endosome acidic environment (4.5–5.5). In addition, the specific precipitation reaction identified that Zn^{2+} was the acid hydrolysis products of ZnO QDs (Fig. S2). Thus, it could deduce that ZnO QDs with well water-dispersible property and appropriate particle size as well as acidic dissolution ability could perfectly act as the gate-keepers for preventing the premature drug release.

3.2. Preparation and characterization of the HMC-SS-ZnO nanoparticles

The morphology of HMC nanoparticles was characterized by TEM (Fig. S3A), where HMC showed the uniform and monodispersed spherical feature with hierarchical hollow mesoporous structure resulting in tremendous drug loading capacity. Also, the mean particle size of HMC was about 140 nm with a 40 nm mesoporous shell. To characterize the multifunctional modifications of HMC, TEM-EDX mapping, FT-IR and XPS were employed. As shown the element mapping analysis in Fig. 2A (b-e) and S4C (a-c), the C element was the parent skeleton of HMC, in which the hollow structure was apparent. The S element was distributed above the HMC surface, indicating the successful grafting of disulfide bonds. Furthermore, the Zn element was evenly distributed in the outermost layer, indicating the successful construction of HMC-SS-ZnO. The mass fraction of each element was 79.50% of C, 0.16% of N, 16.55% of O, 0.51% of S, and 3.28% of Zn, respectively (Table S2), and the energy spectra dot measurement results were shown in Fig. S4. Compared with naked HMC, bands at 1717.5 cm^{-1} appeared in HMC-COOH and HMC-SS-COOH, which were attributed to the C—O stretching vibration of carboxyl groups. Subsequently, 1717.5 cm^{-1} bands disappeared while 1580 cm^{-1}, 1050 cm^{-1}, and 488 cm^{-1} three distinct peaks emerged after NH_2-ZnO QDs conjugation, which were associated to the Si—O—Si stretch vibration, N—H bend vibration and Zn—O stretching vibra-

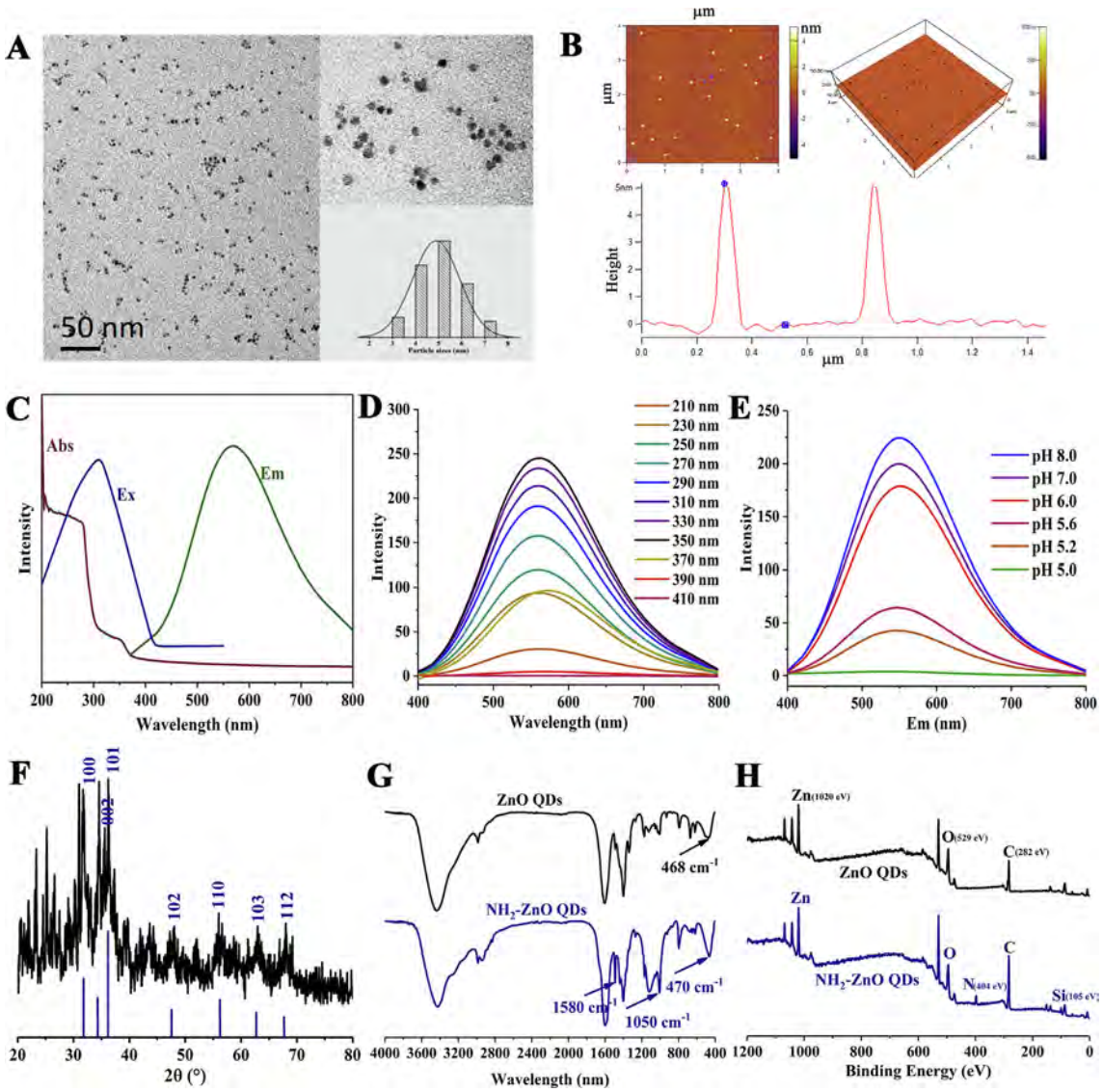

Fig. 1. (A) TEM images of ZnO QDs; (B) AFM images, three-dimensional AFM results, and height profile; (C) UV–Vis absorption spectrum, excitation and emission spectra; (D) PL emission spectra under different excitation wavelengths; (E) Fluorescence spectra of NH_2-ZnO QDs at different pH values; (F) XRD patterns of ZnO QDs and standard pattern of ZnO; (G) XPS patterns; (H) FT-IR spectra.

tion, respectively (Fig. 2C). Similar XPS results were exhibited in Fig. 2D and details in Table S3. In the HMC-COOH, the element C and O were peaking at 284 mV and 532 mV with proportions of 87.17% and 10.47%, respectively. For HMC-SS-COOH, the S 2p peak appeared at 167 eV with the proportion of 0.82% additionally. After NH_2-ZnO QDs conjugation, peaks at 1021 eV, 397 eV and 100 eV were coexisting in HMC-SS-ZnO, attributed to Zn 2p, N 1s and Si 2p, separately. These all results indicated the successful preparation of HMC-SS-ZnO. The results of specific surface area, pore size and total pore volume of the nanoparticles were gathered from nitrogen adsorption-desorption measurements (Fig. 2E, F). After each modification procedure, all three parameters of the HMC materials decreased by degrees (Table S4). Further, the changes of Zeta potential also proved each successful modification (Fig. 2B). Meanwhile, the dark spots on the exterior edges of the nanoparticles appeared in the TEM micrograph (Fig. 2A(a)). However, the mesoporous structures of the HMC shells could be apparently observed again after the HMC-SS-ZnO being incubated in PBS at pH 5.0 for 2 h (Fig. 2G illustration), further manifesting the favorable pH sensitivity of the ZnO QDs as gate-keepers. Additionally, the dynamic light scattering results (Fig. 2G) recognized the hydrodynamic diameter of HMC-SS-ZnO was 287 nm, which was slightly larger compared to HMC-COOH of 209 nm, whereas it suffered a cutback to 213 nm after acidic treatment, and these supplements explained the above conclusions. These phenomena demonstrated that the HMC nanoparticles possessed of proper particle size for tumor passive targeting, and could achieve a significant drug loading capacity due to their large specific surface area. Meanwhile, ZnO QDs and disulfide bonds as the gatekeepers could be opened encountering the tumor microenvironment of pH and redox for stimuli-triggered controlled drug release.

3.3. In vitro photothermal effect and photostability of HMC-SS-ZnO

UV–Vis-NIR scanning spectra results showed that both HMC-COOH and HMC-SS-ZnO had strong UV–Vis-NIR absorption at NIR short-wave band (Fig. 3A) unveiling their potential NIR photothermal conversion abilities. As shown in Fig. 3B and C, the photothermal effect of HMC-SS-ZnO showed concentration-dependent, irradiation time-dependent and power density-

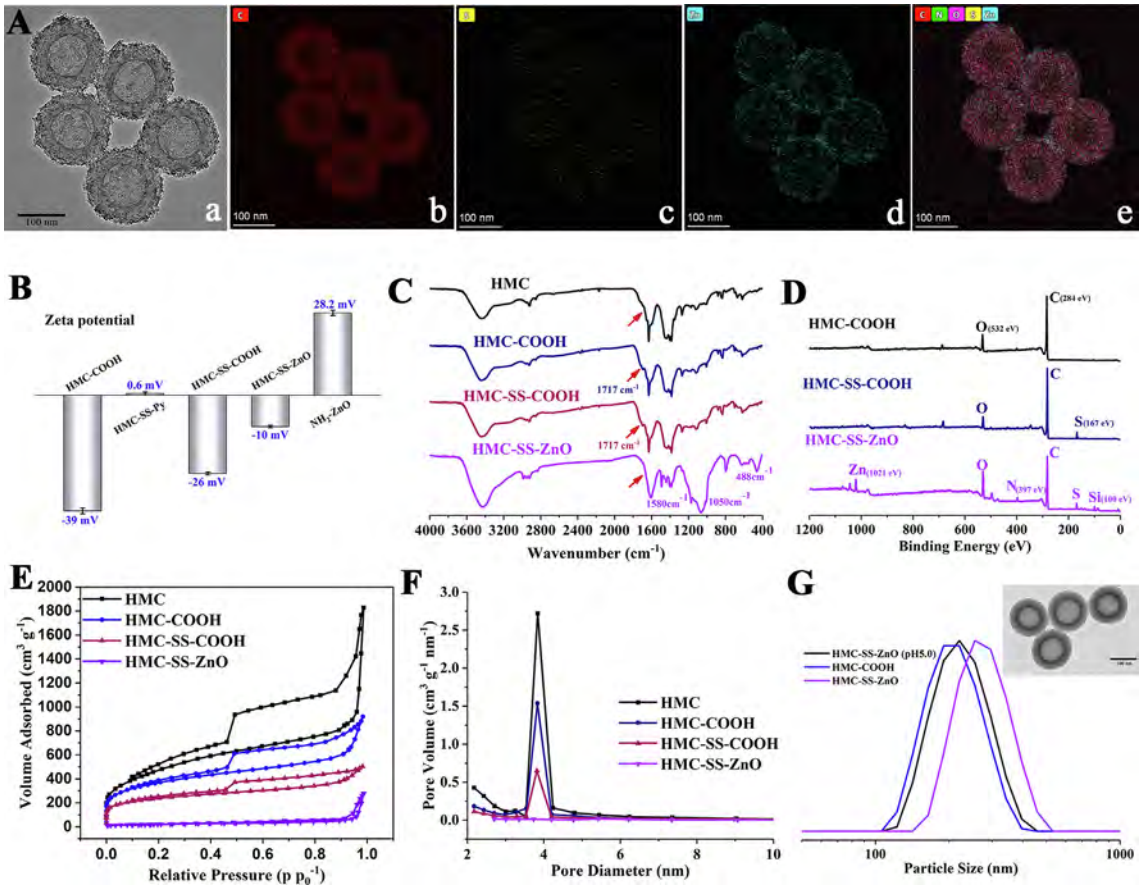

Fig. 2. (A) TEM image of HMC-SS-ZnO (a), corresponding C (b), S (c), and Zn (d) EDX mappings, and merged image (e) including C, N, O, S, and Zn; (B) Zeta potentials results (n = 3); (C) FT-IR spectra, (E) nitrogen adsorption/desorption isotherms and (F) pore size distribution curves; (D) XPS patterns; (G) Size distributions of HMC-COOH, HMC-SS-ZnO and HMC-SS-ZnO after incubation in PBS (pH 5.0) for 2 h (Illustration: TEM image of the last group).

dependent patterns. The temperature of the HMC-SS-ZnO increased expeditiously under continuous irradiation, while no evident change was detected in distilled water (Fig. S5). Additionally, for the photothermal stability of HMC-SS-ZnO, Fig. 3E displayed that almost no observable attenuation took place during the irradiation and natural cooling for 5 times repeats. Furthermore, the photothermal conversion efficiency (η) was 29.7% shown in Fig. 3F and inserted illustration. These results indicated the excellent photostability and constant photothermal conversion capacity of HMC-SS-ZnO.

3.4. Dispersion stability and hemocompatibility validation of HMC-SS-ZnO

For the dispersion stability test, the HMC-COOH and HMC-SS-ZnO nanoparticles were uniformly dispersed in water and PBS (pH 7.4), separately. Fig. 3G showed that the hydrodynamic diameters and PDIs of HMC-COOH and HMC-SS-ZnO nanoparticles were relatively constant in water dispersion medium as standing time going by. However, HMC-SS-ZnO possessed of better dispersion stability in the simulated body fluid conditions, which was contributed by the electrostatic repulsion force and steric hindrance effect of outer hydrophilic ZnO QDs (Fig. 3H). In addition, hemocompatibility was studied to evaluate the biosecurity of HMC-SS-ZnO nanoparticles to blood cells. As displayed in Fig. 3I, the hemolysis percentage of HMC-SS-ZnO nanoparticles was pretty low (1.78% ± 0.15%), and no obvious hemolysis phenomenon was seen after 5 h stilled standing (Fig. S6). These results proved that HMC-SS-ZnO was adequately safe for drug delivery.

3.5. Drug loading capacity and existing state

To estimate the drug loading capacity of the HMC and physical existing state of Dox in Dox/HMC-SS-ZnO, Dox was loaded in HMC-SS-COOH before NH_2-ZnO QDs capping, driving by the intermolecular forces such as π–π stacking interaction and electrostatic attraction between drug and HMC. Dox loading efficiency of Dox/HMC-SS-ZnO was 43%, which was resulted from the tremendous specific surface area of mesoporous hollow structure, powerful adsorption ability of HMC materials, as well as the considerable noncovalent interactions among molecules. Furthermore, XRD and DSC techniques were employed to determine the physical existing state of Dox in Dox/HMC-SS-ZnO. As shown in Fig. 4A, D, characteristic crystalline diffraction peaks or melting point endothermic peaks of drug emerged in the raw Dox and physical mixture of HMC-SS-ZnO and Dox, while no obvious peak of Dox in crystalline form was observed in the Dox/HMC-SS-ZnO, proving the Dox loaded in the meso-channels existing in non-crystalline form (amorphous state) which was in possession of superior dissolution rate.

3.6. In vitro pH/redox/NIR triple stimuli-responsive drug release

Fig. 4B illustrated the drug release behaviors of Dox/HMC-COOH and Dox/HMC-SS-ZnO in different release media. Both Dox/HMC-COOH and Dox/HMC-SS-ZnO preformed higher Dox release amounts in PBS at pH 5.0 than that in PBS at pH 7.4 due to the electrostatic force between Dox and nanocarriers weakening in acidic condition, which could weaken the intermolecular interaction such

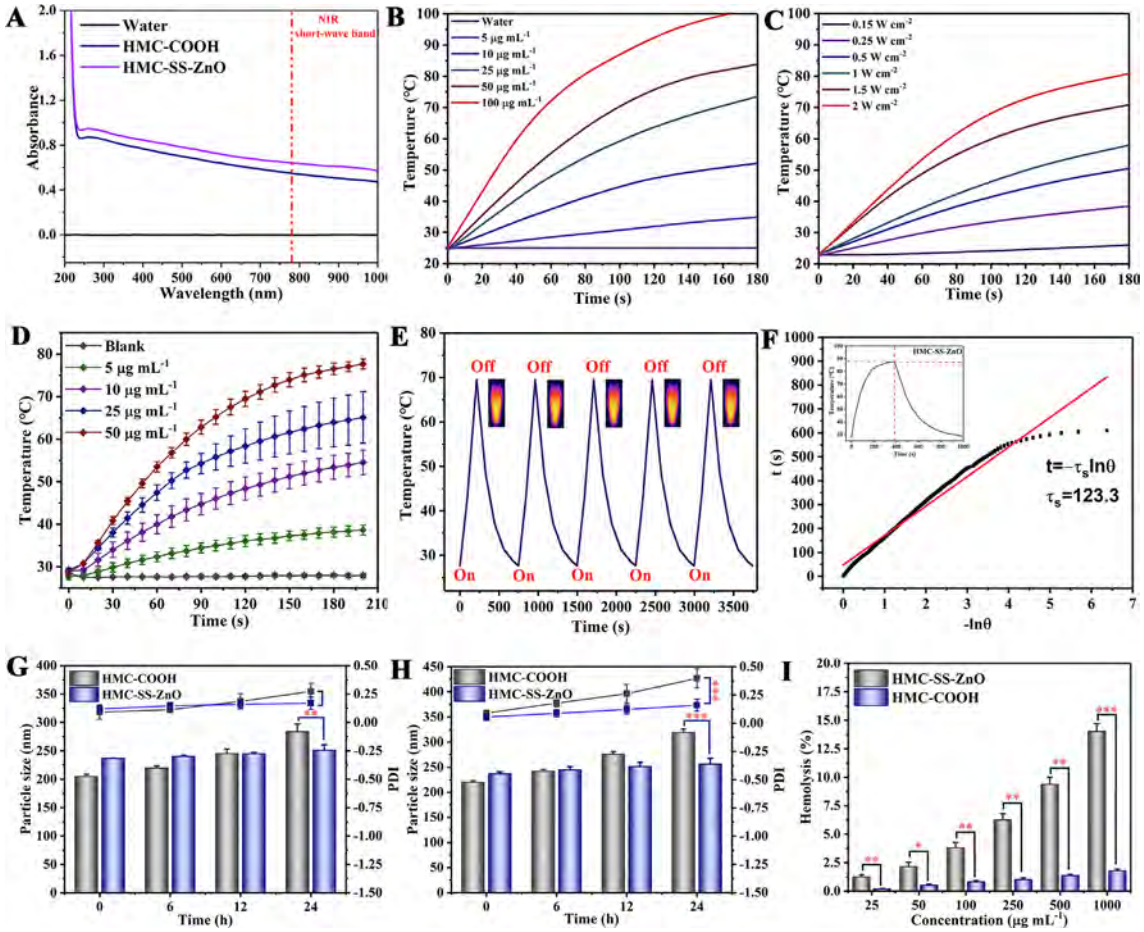

Fig. 3. (A) UV–Vis-NIR scanning spectra (water as control); (B) Photothermal heating profiles of the HMC-SS-ZnO suspensions with series of concentrations. (C) Photothermal heating profiles of the HMC-SS-ZnO suspensions under series of power intensities; (D) Photothermal heating profiles of 4T1 cells (n = 3); (E) Photothermal stability of HMC-SS-ZnO; (F) Linear time data versus -lnθ obtained from the cooling stage of HMC-SS-ZnO photothermal effect curve (Illustration); Particle sizes and PDIs of HMC-COOH and HMC-SS-ZnO dispersed in (G) water and (H) PBS (pH 7.4), respectively (n = 3); (I) Hemolysis percentage of HMC-COOH and HMC-SS-ZnO (n = 3) (*$p < 0.05$, **$p < 0.01$, ***$p < 0.001$).

as π-π stacking and hydrophobic forces and promote drug escaping from the channels. However, in the same pH condition, the cumulative release of Dox from Dox/HMC-SS-ZnO was less and slower than that of Dox/HMC-COOH, which demonstrated that ZnO QDs could not only act as gatekeepers to prevent drug premature, also contribute to the controlled drug release due to their pH sensitivity. Furthermore, the redox sensitivity property of Dox/HMC-SS-ZnO in the drug release was studied. As shown in Fig. 4C, the cumulative release of Dox/HMC-SS-ZnO in PBS at pH 5.0 containing 10 mM GSH was considerably increased and was much higher than in PBS at pH 5.0 without GSH (from 18.86% to 28.62%), whereas no obvious change in Dox/HMC-COOH (from 30.60% to 31.92%), proving the GSH responsive assigned to the disulfide bonds. In order to study the photothermal effect on drug release, Dox/HMC-SS-ZnO and Dox/HMC-COOH were experienced the 808 nm NIR irradiation (1.0 W cm^{-2}) for 3 min during drug release period at 2 h, 6 h and 10 h, respectively. As shown in Fig. 4E, F, terraced and accelerated release patterns were observed in the irradiated points. Finally, the cumulative drug release amount of Dox/HMC-SS-ZnO in 10 mM GSH added pH 5.0 PBS with NIR irradiation was 55.3%, which were 2.5-folder higher than either no GSH (28.62%) or without NIR irradiation (18.86%), exhibiting the NIR and redox synergistic stimuli-responsive character of Dox/HMC-SS-ZnO. In conclusion, Dox/HMC-SS-ZnO drug delivery system possessing of pH/redox/NIR triple stimuli-responsive release properties may effectively utilize the characteristics of tumor microenvironment (TME) for drug accurate delivery.

3.7. Photothermal therapy effect on cytological level

PTT effect of HMC-SS-ZnO on cytological level was studied. As shown in Fig. 3D, cells given different concentrations of HMC-SS-ZnO showed different degrees of temperature increase under continuous NIR irradiation, and no apparent change was found in control group, manifesting that HMC-SS-ZnO taken in 4T1 cells enabled the cells photothermal conversion capacity. In Fig. 5A, most cells incubated with PBS under NIR irradiation and with HMC-SS-ZnO particles without irradiation were alive (green), whereas the red/green fluorescence signal ratio in 4T1 cells was gradually increased along with the extension of irradiation time, demonstrating that HMC-SS-ZnO had the favorable biocompatibility and superior PTT ability.

3.8. Cellular uptake of Dox/HMC-SS-ZnO

Sufficient cellular internalization of Dox/HMC-SS-ZnO in tumor cells is particularly beneficial for effective chemo-photothermal synergistic therapy. As shown in the CLSM results in Fig. 5C, free Dox was mainly localized in the cell nuclei as the result of its high affinity with DNA. Initially, feeble red fluorescence appeared in cytoplasm in cells incubated with Dox/HMC-SS-ZnO, whereas strong red fluorescence was observed in the cytoplasm and cell nuclei after 4 h, indicating that the Dox/HMC-SS-ZnO was availably internalized by 4T1 cells and Dox was gradually released from nanoparticles (Figs. S7 and S8). Moreover, the Dox fluorescence

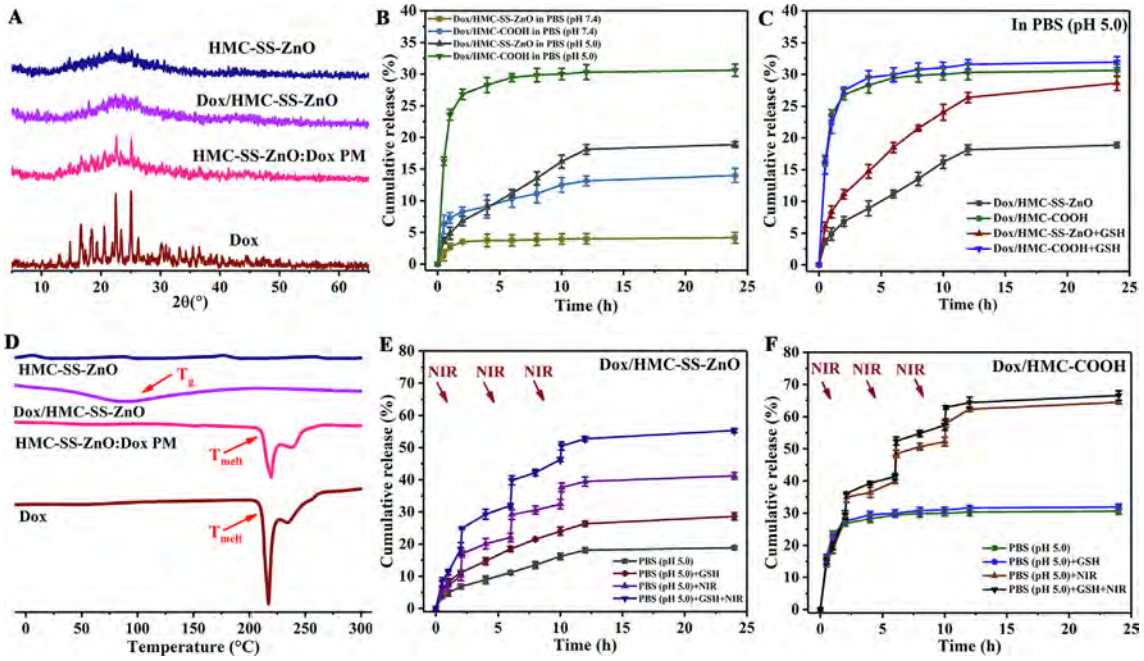

Fig. 4. (A) XRD and (D) DSC patterns; (B) Drug release profiles of Dox/HMC-COOH and Dox/HMC-SS-ZnO in pH 7.4 and pH 5.0 PBS (n = 3); (C) Drug release profiles of Dox/HMC-COOH and Dox/HMC-SS-ZnO in pH 5.0 PBS with/without 10 mM GSH (n = 3); Drug release profiles of (E) Dox/HMC-SS-ZnO and (F) Dox/HMC-COOH with 10 mM GSH and NIR irradiation at 1.0 W cm^{-2} in PBS at pH 5.0, respectively (n = 3).

intensity in Dox/HMC-SS-ZnO + NIR group was further enhanced after treatment with NIR irradiation at 1.0 W cm^{-2} for 3 min, resulting from the local hyperthermia that could not only impact the permeability and fluidity of cell membrane to increase cellular endocytosis, but also accelerate molecular thermal motion to promote drug release. Furthermore, FCM was employed to quantificationally evaluate the cellular uptake of Dox/HMC-SS-ZnO by monitoring Dox fluorescence in cells (Fig. 5D), and the results were consistent with the CLSM results.

3.9. Cytotoxicity test

Subsequently, the cytotoxicity of Dox/HMC-SS-ZnO against 4T1 breast cells under NIR irradiation was evaluated by MTT assay for the examination of chemo-photothermal synergistic therapy. In Fig. 6A, HMC-SS-ZnO within the experimental concentration range displayed the high cell viability (>90%), suggesting that HMC-SS-ZnO was safe and biocompatible. For chemotherapy alone, a drug concentration-dependent cell inhibition rate was observed. Besides, NIR irradiation had no significant effect on the cytotoxicity of free Dox group, and the cell viabilities and IC_{50} values were similar, suggesting that NIR laser irradiation could not be toxic to the cells (Table 1). Meanwhile, PTT alone performed apparent cytotoxicity at a concentration of 10 μg mL^{-1} and the cell viability decreased to nearly 50%. As expected, compared with chemotherapy or PTT alone, the 4T1 cells treated with Dox/HMC-SS-ZnO under NIR irradiation exhibited a superior combination therapeutic effect of chemo-photothermal therapy with a cell inhibition of 75.2% (Fig. 6B). The combination index (CI), commonly used for evaluating the synergistic efficacy of the combination therapy, was calculated as 0.532, demonstrating that the chemo-photothermal combination therapy based on Dox/HMC-SS-ZnO showed an efficient synergistic therapeutic effect in tumor [61]. This result might be explained by the fact that the high temperature could damage tumor cells and increase the sensitivity of the cells to chemotherapeutic drugs, thereby causing the maximal cytotoxicity.

3.10. Cell apoptosis test

FCM was used for cell apoptosis test to explore the mechanism of chemo-photothermal therapy effect of Dox/HMC-SS-ZnO. As shown in Fig. 6C, cells in free Dox and Dox/HMC-SS-ZnO groups endured apoptosis and slightly necrosis with about 20% cells in early apoptotic stage and about 35% cells in late apoptotic stage, respectively. The fact was attributed to that Dox might cause cytotoxicity by binding to DNA and produce a large number of free radicals which may interfere with mitochondrial functions leading to mitochondrial dependent apoptosis in tumor. However, the cells in PBS and PBS + NIR groups exhibited no observable apoptosis phenomenon, versifying that NIR laser was safe for normal biological tissues, which was consistent with MTT results. Meanwhile, cells treated with PTT alone induced apoptosis rate up to 40% possibly due to the reactive oxygen species, endoplasmic reticulum stress, mitochondria, and caspase pathways related cell apoptosis activated by the hyperthermia [62,63]. Expectedly, with the extension of irradiation time, the apoptosis rate of tumor cells gradually increased (Fig. 5B), further attesting the excellent PTT capacity of Dox/HMC-SS-ZnO. Spectacularly, apoptosis rate in synergistic therapy group remarkably increased to 98.9% during such a short therapeutic period, convincingly demonstrating the powerful dual-model antitumor function of Dox/HMC-SS-ZnO with chemo-photothermal synergistic therapy.

3.11. In vitro MCTSs lethality test

To investigate the effective lethality of Dox/HMC-SS-ZnO to the solid tumor of breast cancer, MCTSs model was built to simulate the solid tumor for further study. As shown in Fig. 6D and E, a higher red fluorescence intensity (dead cells) was observed after chemo-photothermal synergistic therapy compared to either chemotherapy or PTT alone. Percentage of dead cells in synergistic therapy group was about 1.5-fold than two individual therapy regimens. Additionally, microscopic data displayed the morphology changes of MCTSs in the one-week treatments (Fig. S9). Compared

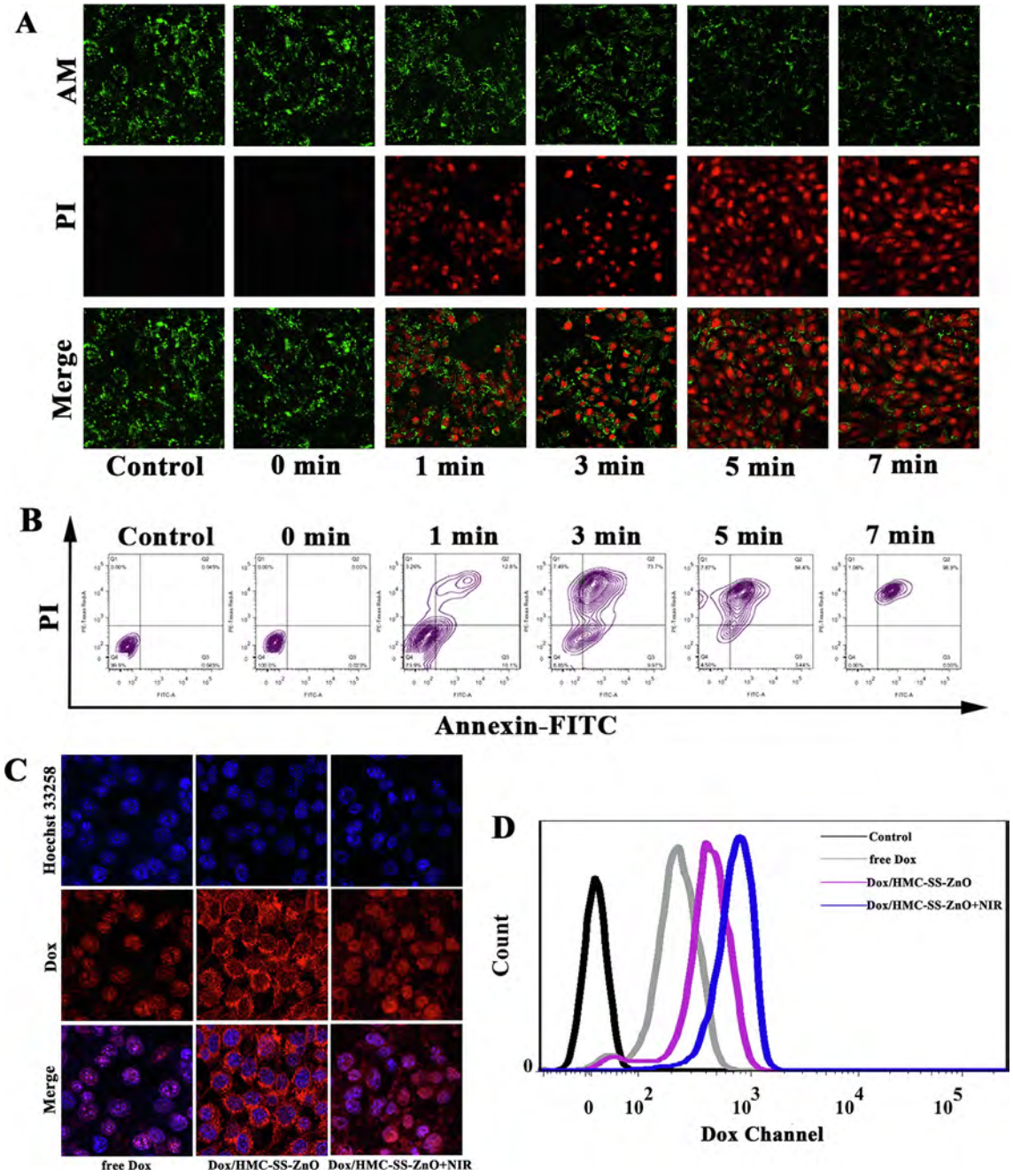

Fig. 5. (A) Fluorescence images of 4T1 cells incubated with HMC-SS-ZnO with NIR irradiation (1.0 W cm^{-2}) for different times and co-stained with Calcein AM (live cells, green) and PI (dead cells, red); (B) FCM analysis of cell apoptosis induced by NIR irradiation with different times, performed using Annexin V-FITC/PI staining; Cellular uptake: (C) CLSM images and (D) FCM analysis of 4T1 cells incubated with free Dox and Dox/HMC-SS-ZnO ± NIR for 4 h. (For interpretation of the references to color in this figure legend, the reader is referred to the web version of this article.)

with the control groups, MCTSs in each treatment group suffered certain collapsed and dissociated, especially in combination therapy group. Tumor spheroids almost completely disappeared after five-day treatment, which was accordance with other results in above. So far, these inspiring findings proved the optimal characteristics of Dox/HMC-SS-ZnO delivery system, and well prepared for the subsequent trials *in vivo*.

3.12. Biodistribution study

To investigate the characteristics of drug biodistribution after dosing into blood, free Dox and Dox/HMC-SS-ZnO with same drug amount (10 mg mL^{-1}) were injected into mice *via* caudal vein, and the Dox fluorescence signals were detected at 2, 6 and 12 h, respectively. As displayed in Fig. 7A and B, free Dox was distributed in all the major organs after administration, especially in the heart and kidney. In fact, Dox tends to target and injure the mitochondria in cardiomyocytes, causing certain cardiac toxicity, and easily leads to drug-induced nephropathy ascribing the powerful excretory function of kidneys [64,65]. Moreover, as previously recognized that the half-life of Dox using alone was very short which may be responsible for the sharp decline in the drug amount in tumor sites with the prolongation of injection time. As the functionalized nanoparticles encountered the tumor microenvironment, where

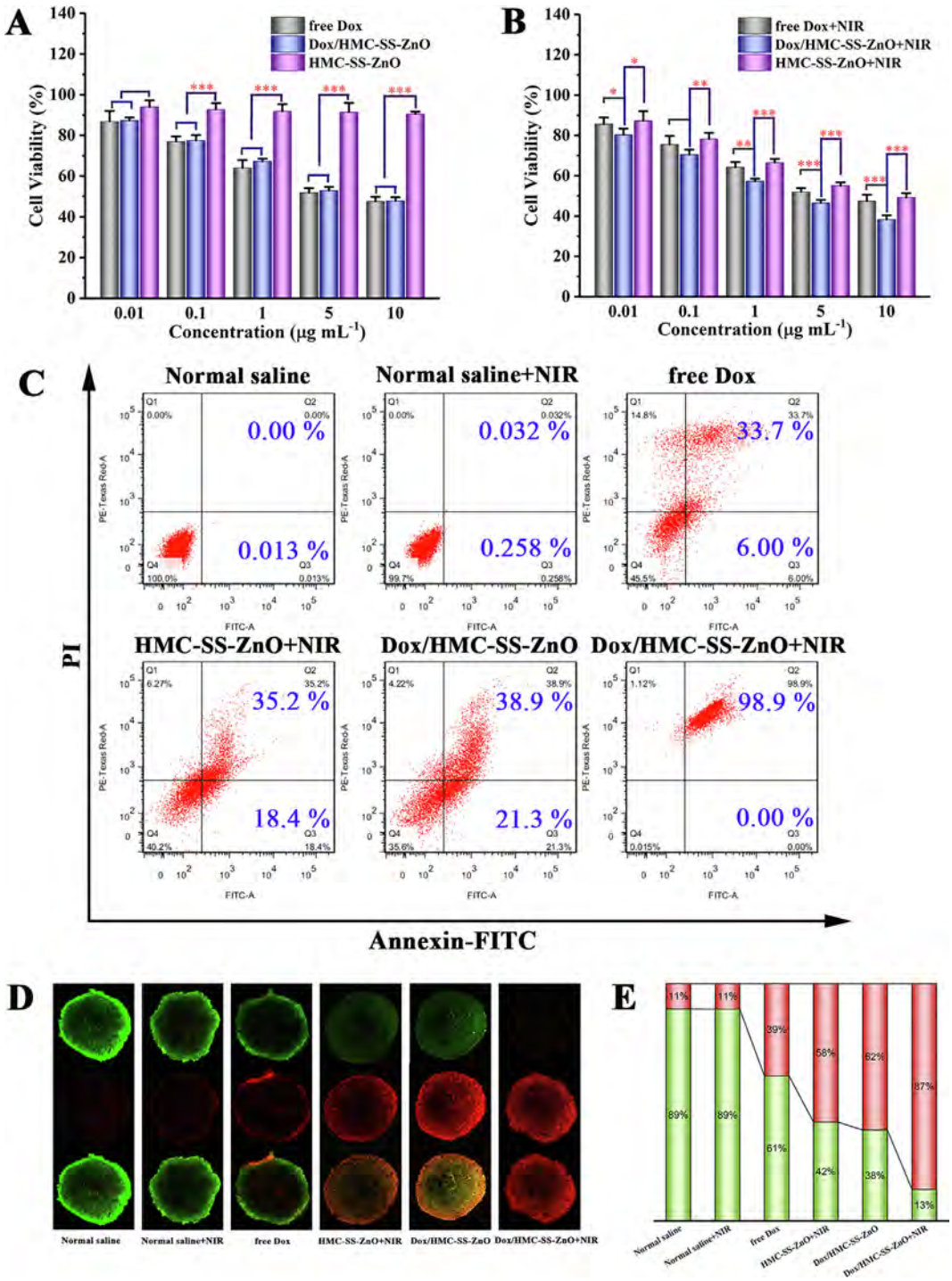

Fig. 6. The cell viabilities of 4T1 cells (B) with or (A) without NIR laser irradiation (n = 5); (C) FCM analysis of 4T1 cells' apoptosis induced by different therapeutic treatments, performed using Annexin V-FITC/PI staining; (D) MCTSs lethality test: Fluorescence images of MCTSs with different pretreatments and (E) the corresponding cell dead/live quantitative analysis.

Table 1
IC_{50} values of HMC-SS-ZnO, free Dox and Dox/HMC-SS-ZnO ± NIR against 4T1 cells.

Samples	IC_{50} (μg mL^{-1})	
	without NIR irradiation	NIR irradiation
HMC-SS-ZnO	–	9.957
free Dox	6.950	7.082
Dox/HMC-SS-ZnO	8.197	2.393

the gating switches were triggered, Dox was released from the nanocarriers with appearing the gradually enhanced fluorescence signals at the tumor sites. Compared to free Dox, Dox/HMC-SS-ZnO significantly prolonged intratumor retention time of drug performing the stronger fluorescent intensity in tumors within 12 h and maximum amount at 6 h. Besides, the elevated temperature generated by NIR irradiation could further promote the endocytosis internalization and intracellular drug release. In summary, aiming at the shortages of free Dox treatment, Dox/HMC-SS-ZnO with

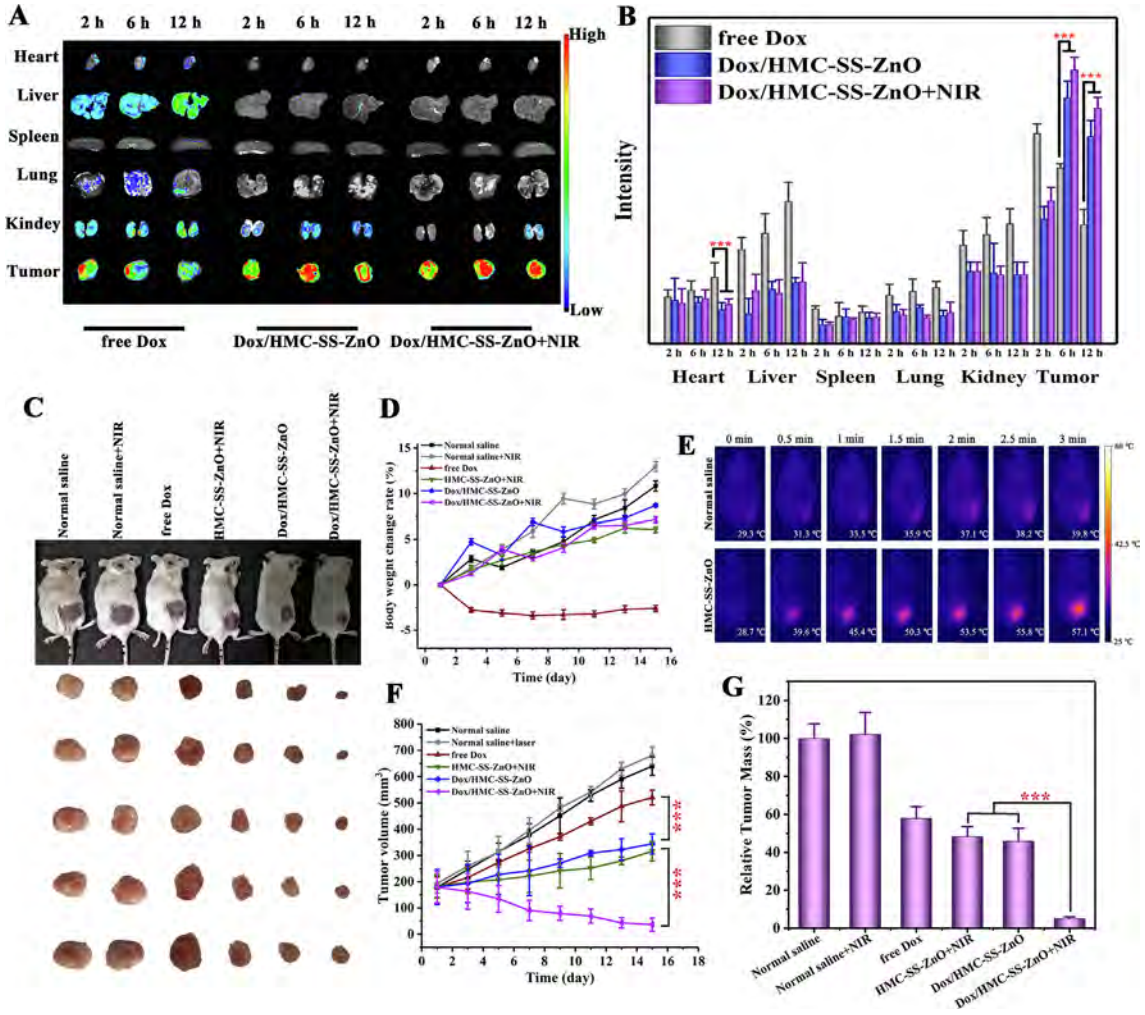

Fig. 7. (A) Fluorescence imaging of isolated main organs; (B) Fluorescence intensity semiquantification of the Dox biodistribution in tumor-bearing mice at 2, 6 and 12 h (n = 3); (C) Photographs of excised tumors (n = 5); (D) Body weight evolution curves (n = 5). (E) Thermography photographs of mice after injection of normal saline and HMC-SS-ZnO under NIR irradiation at 1.0 W cm^{-2}; (F) Profiles of relative tumor volume (n = 5). (G) Relative tumor mass of excised tumors (n = 5).

NIR irradiation combined therapeutic regimen had the advantages of effect-enhancing and toxicity-reducing.

3.13. In vivo antitumor therapy and thermal imaging

Encouraged by the attractive synergistic therapeutic effect and superior biocompatibility of HMC-SS-ZnO *in vitro* experiments, we further investigated the antitumor effects *in vivo* based on mammary adenocarcinoma (4T1) tumor-bearing modelling mice. As displayed in Fig. 7G, compared post-treatment to pretherapy, tumors of mice in the normal saline ± NIR groups increased significantly. In contrast, tumors of mice in other treatment groups decreased to different degrees, and the tumor-inhibition rates for free Dox, PTT alone, Dox/HMC-SS-ZnO and the Dox/HMC-SS-ZnO + NIR were 23.5%, 49.5%, 53.6% and 94.6%, respectively. Similarly, the typical photographs of tumors (Fig. 7C) and the tumor mass-time curves (Fig. 7F) after 15 days treatment additionally demonstrated the more outstanding therapeutic effect of Dox/HMC-SS-ZnO with NIR irradiation than any monotherapy (chemotherapy or PTT). Meanwhile, the body weight of mice was measured and no meaningful body weight loss was observed during the treatment period except for the mice in free Dox group (Fig. 7D), indicating the certain toxicity of the free Dox.

Additionally, when mice treated with HMC-SS-ZnO, the local tumor temperature was elevated by more than 20 °C after NIR irradiation, which was totally high enough to ablate the tumor focus (Fig. 7E). To further analyze the antitumor mechanism of synergistic therapeutic group, the stripped tumors were sectioned and stained with H&E. Images exhibited considerably enhanced cell necrosis and apoptosis for the synergistic therapy group compared with others (Fig. 8). In conclusion, based on above outcomes, we can confirm that Dox/HMC-SS-ZnO possesses gigantic potential as an ideal NIR-induced dual-model antitumor nanoplatform for cancer therapy.

3.14. Biocompatibility

To further verify the potential toxicity on major organs of experimental animals, the heart, liver, spleen, lung and kidney were stripped out and stained with H&E after 15-day therapy for further histological analysis (Fig. 8). No apparent pathological change in major organs was observed in all treatment groups except for the free Dox group, which exhibited mild cardiotoxicity. So far, we may speculate that our Dox/HMC-SS-ZnO nanoplatform could not only weaken the cardiac toxicity by decreasing the accu-

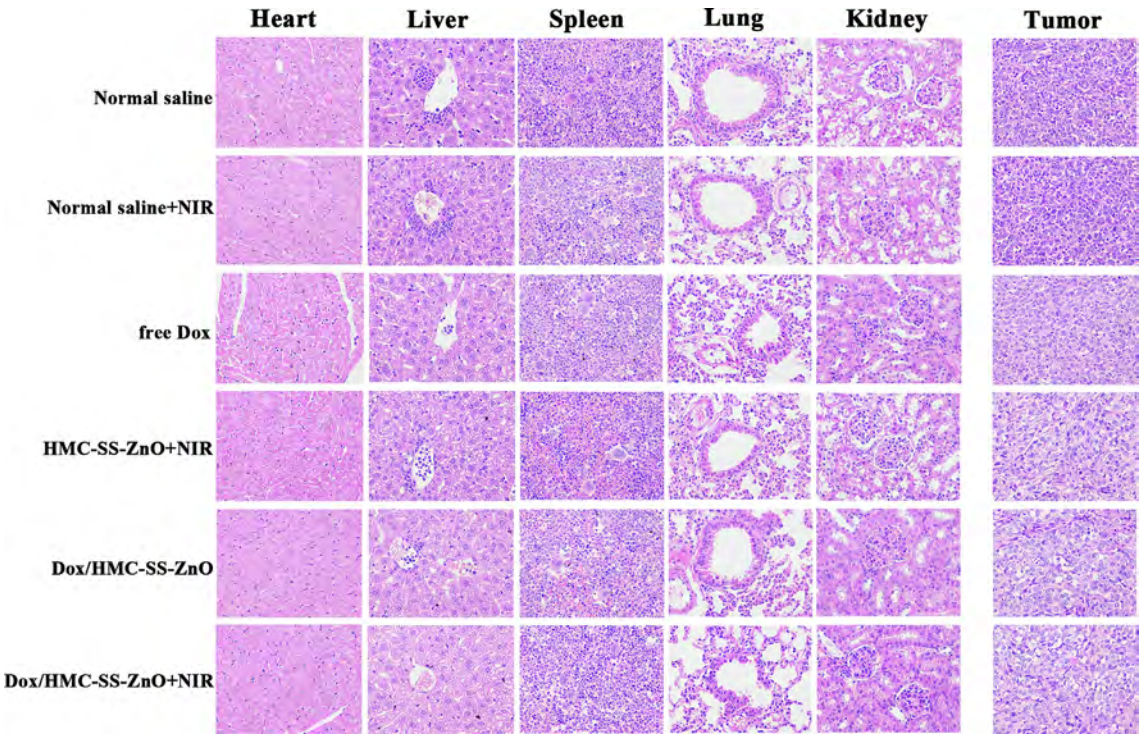

Fig. 8. H&E staining photographs of heart, liver, spleen, lung, kidney and tumor from different treatment groups.

mulation of free Dox in the heart, but also possess good biocompatibility and superior antitumor potential.

4. Conclusion

In summary, a novel multifunctional nanoplatform was developed based on HMC to solve the inefficiency and toxicity problems in traditional chemotherapy. Compared with common nanocarriers and NIR photothermal conversion agents [24,25,34–39,66], HMC with a large specific surface area and hollow mesoporous structure could be used not only as the drug depots to ensure the high loading capacity, but also as a PTT carrier to realize the chemo-photothermal synergistic therapy. Moreover, acid-dissoluble, biocompatible and thermostable ZnO QDs as the gatekeepers were linked to HMC-COOH via disulfide bonds to endow the system with pH/redox/NIR triple stimuli-responsive properties for accurate drug delivery and controlled drug release in tumor sites. Dox/HMC-SS-ZnO possess double benefits with a high drug loading efficiency of 43% and an outstanding photothermal conversion efficiency of 29.7%. Experiments on cytological level, MCTSs' level and animal level comprehensively verified the dual model chemo-photothermal synergistic antitumor efficacy with a CI of 0.532. The key improvement in this study is that clustering all the functional elements in one system to realize a satisfying drug loading efficiency, tumor specific, intracellular stimuli-sensitive, drug controlled release and chemo-photothermal synergistic therapy [9,15,17,67]. All the results *in vitro* and *in vivo* experiments suggested that such an effect-enhancing and toxicity-reducing nanoplatform offered a promising prospect for our fight against cancer in a safer, higher-performance strategy.

Acknowledgements

This work was supported by National Natural Science Foundation of China (Nos. 81603058 and 81473165) and Youth Project of Liaoning Provincial Education Department of China (No. 2017LQN20).

Declaration of Competing Interest

The authors declared that there is no conflict of interest.

Appendix A. Supplementary material

Supplementary data to this article can be found online at https://doi.org/10.1016/j.jcis.2019.09.120.

References

[1] C.E. DeSantis, C.C. Lin, A.B. Mariotto, R.L. Siegel, K.D. Stein, J.L. Kramer, R. Alteri, A.S. Robbins, A. Jemal, CA Cancer J. Clinic. 64 (2014) 252.
[2] M. Karimi, A. Ghasemi, P. Sahandi Zangabad, R. Rahighi, S.M. Moosavi Basri, H. Mirshekari, M. Amiri, Z. Shafaei Pishabad, A. Aslani, M. Bozorgomid, D. Ghosh, A. Beyzavi, A. Vaseghi, A.R. Aref, L. Haghani, S. Bahrami, M.R. Hamblin, Chem. Soc. Rev. 45 (2016) 1457.
[3] S.F. Medeiros, A.M. Santos, H. Fessi, A. Elaissari, Int. J. Pharm. 403 (2011) 139.
[4] K.D. Miller, R.L. Siegel, C.C. Lin, A.B. Mariotto, J.L. Kramer, J.H. Rowland, K.D. Stein, R. Alteri, A. Jemal, CA Cancer J. Clinic. 66 (2016) 271.
[5] D. Peer, J.M. Karp, S. Hong, O.C. Farokhzad, R. Margalit, R. Langer, Nat. Nanotechnol. 2 (2007) 751.
[6] J. Yu, X. Chu, Y. Hou, Chem. Commun. 50 (2014) 11614.
[7] A. Hervault, A.E. Dunn, M. Lim, C. Boyer, D. Mott, S. Maenosono, N.T. Thanh, Nanoscale 8 (2016) 12152.
[8] Z. Li, D. Kai, Z. Chen, J. Ren, X. Qu, Carbon 82 (2015) 479.
[9] I.R. Fernando, D.P. Ferris, M. Frasconi, D. Malin, E. Strekalova, M.D. Yilmaz, M. W. Ambrogio, M.M. Algaradah, M.P. Hong, X. Chen, Nanoscale 7 (2015) 7178.
[10] S.M. Lee, H.J. Kim, S.Y. Kim, M.K. Kwon, S. Kim, A. Cho, M. Yun, J.S. Shin, K.H. Yoo, Biomaterials 35 (2014) 2272.
[11] Y. Pan, L. Zhang, L. Zeng, W. Ren, X. Xiao, J. Zhang, L. Zhang, A. Li, G. Lu, A. Wu, Nanoscale 8 (2016) 878.
[12] Y. Xing, J. Zhang, F. Chen, J. Liu, K. Cai, Nanoscale 9 (2017) 8781.
[13] Y. Li, X. Xu, X. Zhang, Y. Li, Z. Zhang, Z. Gu, ACS Nano 11 (2017) 416.
[14] X. Huang, I.H. El-Sayed, W. Qian, M.A. El-Sayed, J. Am. Chem. Soc. 128 (2006) 2115.
[15] Q. Tian, F. Jiang, R. Zou, Q. Liu, Z. Chen, M. Zhu, S. Yang, J. Wang, J. Wang, J. Hu, ACS Nano 5 (2011) 9761.

[16] C. Wang, H. Xu, C. Liang, Y. Liu, Z. Li, G. Yang, L. Cheng, Y. Li, Z. Liu, ACS Nano 7 (2013) 6782.
[17] J. Zhou, Z. Lu, X. Zhu, X. Wang, Y. Liao, Z. Ma, F. Li, Biomaterials 34 (2013) 9584.
[18] F. Wu, M. Zhang, H. Lu, D. Liang, Y. Huang, Y. Xia, Y. Hu, S. Hu, J. Wang, X. Yi, ACS Appl. Mater. Interfaces 10 (2018) 21939.
[19] K. Cheng, X.Q. Yang, X.S. Zhang, J. Chen, J. An, Y.Y. Song, C. Li, Y. Xuan, R.Y. Zhang, C.H. Yang, Adv. Funct. Mater. 28 (2018) 1803118.
[20] Y. Zhang, L. Yang, L. Yan, G. Wang, A. Liu, Coord. Chem. Rev. 391 (2019) 69.
[21] Y. Zhang, G. Wang, L. Yang, F. Wang, A. Liu, Coord. Chem. Rev. 370 (2018) 1.
[22] W. Chen, J. Ouyang, H. Liu, M. Chen, K. Zeng, J. Sheng, Z. Liu, Y. Han, L. Wang, J. Li, L. Deng, Y.N. Liu, S. Guo, Adv. Mater. 29 (2017) 1603864.
[23] M.Y. Peng, D.W. Zheng, S.B. Wang, S.X. Cheng, X.Z. Zhang, ACS Appl. Mater. Interfaces 9 (2017) 13965.
[24] H.P. Tham, H. Chen, Y.H. Tan, Q. Qu, S. Sreejith, L. Zhao, S.S. Venkatraman, Y. Zhao, Chem. Commun. 52 (2016) 8854.
[25] S. Shen, H. Tang, X. Zhang, J. Ren, Z. Pang, D. Wang, H. Gao, Y. Qian, X. Jiang, W. Yang, Biomaterials 34 (2013) 3150.
[26] J. Yang, J. Choi, D. Bang, E. Kim, E.K. Lim, H. Park, J.S. Suh, K. Lee, K.H. Yoo, E.K. Kim, Y.M. Huh, S. Haam, Angew. Chem. Int. Ed. 50 (2011) 441.
[27] Y. Liu, K. Ai, J. Liu, M. Deng, Y. He, L. Lu, Adv. Mater. 25 (2013) 1353.
[28] L. Cheng, K. Yang, Q. Chen, Z. Liu, ACS Nano 6 (2012) 5605.
[29] X.C. Qin, Z.Y. Guo, Z.M. Liu, W. Zhang, M.M. Wan, B.W. Yang, J. Photochem. Photobiol. B Biol. 120 (2013) 156.
[30] Y.W. Chen, Y.L. Su, S.H. Hu, S.Y. Chen, Adv. Drug Deliv. Rev. 105 (2016) 190.
[31] L. Wang, J. Shi, X. Jia, R. Liu, H. Wang, Z. Wang, L. Li, J. Zhang, C. Zhang, Z. Zhang, Pharm. Res. 30 (2013) 2757.
[32] L. Hou, X. Yang, J. Ren, Y. Wang, H. Zhang, Q. Feng, Y. Shi, X. Shan, Y. Yuan, Z. Zhang, Int. J. Nanomed. 11 (2016) 607.
[33] X.T. Liu, X.Y. Mu, X.L. Wu, L.X. Meng, W.B. Guan, Y.Q. Ma, H. Sun, C.J. Wang, X.F. Li, Biomed. Environ. Sci. 27 (2014) 676.
[34] J. Gu, S. Su, Y. Li, Q. He, J. Shi, Chem. Commun. 47 (2011) 2101.
[35] Y. Fang, D. Gu, Y. Zou, Z. Wu, F. Li, R. Che, Y. Deng, B. Tu, D. Zhao, Angew. Chem. Int. Ed. 49 (2010) 7987.
[36] J. Zhu, L. Liao, X. Bian, J. Kong, P. Yang, B. Liu, Small 8 (2012) 2715.
[37] T.W. Kim, P.W. Chung, M. Slowing II, E.S. Tsunoda, V.S. Lin Yeung, Nano Lett. 8 (2008) 3724.
[38] T.Y. Ma, L. Liu, Z.Y. Yuan, Chem. Soc. Rev. 42 (2013) 3977.
[39] G. Xu, S. Liu, H. Niu, W. Lv, R.A. Wu, RSC Adv. 4 (2014) 33986.
[40] L. Wang, Y. Wang, J. Hao, S. Dong, Biomacromolecules 18 (2017) 1029.
[41] A. Verma, J.M. Simard, J.W. Worrall, V.M. Rotello, J. Am. Chem. Soc. 126 (2004) 13987.
[42] J. Zhao, J. Liu, S. Xu, J. Zhou, S. Han, L. Deng, J. Zhang, J. Liu, A. Meng, A. Dong, ACS Appl. Mater. Interfaces 5 (2013) 13216.
[43] J. Ding, J. Chen, D. Li, C. Xiao, J. Zhang, C. He, X. Zhuang, X. Chen, J. Mater. Chem. B 1 (2012) 69.
[44] J. Li, M. Huo, J. Wang, J. Zhou, J.M. Mohammad, Y. Zhang, Q. Zhu, A.Y. Waddad, Q. Zhang, Biomaterials 33 (2012) 2310.
[45] X. Zhang, Y. Huang, W. Zhao, Y. Chen, P. Zhang, J. Li, R. Venkataramanan, S. Li, Mol. Pharm. 11 (2014) 2807.
[46] H. Xiang, H. Chen, H.P. Tham, S.Z.F. Phua, J.-G. Liu, Y. Zhao, ACS Appl. Mater. Interfaces 9 (2017) 27553.
[47] J. Zhao, Y. Yang, X. Han, C. Liang, J. Liu, X. Song, Z. Ge, Z. Liu, ACS Appl. Mater. Interfaces 9 (2017) 23555.
[48] Q. Gan, X. Lu, W. Dong, Y. Yuan, J. Qian, Y. Li, J. Shi, C. Liu, J. Mater. Chem. 22 (2012) 15960.
[49] Y. Chen, Q. Yin, X. Ji, S. Zhang, H. Chen, Y. Zheng, Y. Sun, H. Qu, Z. Wang, Y. Li, Biomaterials 33 (2012) 7126.
[50] K. Miyata, M. Oba, M. Nakanishi, S. Fukushima, Y. Yamasaki, H. Koyama, N. Nishiyama, K. Kataoka, J. Am. Chem. Soc. 130 (2008) 16287.
[51] X. Li, X. Wang, L. Sha, D. Wang, W. Shi, Q. Zhao, S. Wang, ACS Appl. Mater. Interfaces 10 (2018) 19386.
[52] Q. Zhao, Y. Yang, H. Wang, W. Lei, Y. Liu, S. Wang, J. Colloid Interface Sci. 554 (2019) 239.
[53] N. Hao, L. Li, F. Tang, ACS Appl. Mater. Interfaces 8 (2016) 29208.
[54] P. Srivastava, S.K. Hira, D.N. Srivastava, U. Gupta, P. Sen, R.A. Singh, P.P. Manna, ACS Biomater. Sci. Eng. 3 (2017) 3376.
[55] J. Fang, Y. Liu, Y. Chen, D. Ouyang, G. Yang, T. Yu, Int. J. Nanomed. 13 (2018) 5991.
[56] X. Wang, X. Li, Y. Mao, D. Wang, Q. Zhao, S. Wang, J. Colloid Interface Sci. 552 (2019) 639.
[57] M. Martínez-Carmona, Y. Gun'ko, M. Vallet-Regí, Nanomaterials 8 (2018) 268.
[58] C. Li, Z. Zang, C. Han, Z. Hu, X. Tang, J. Du, Y. Leng, K. Sun, Nano Energy 40 (2017) 195.
[59] F. Muhammad, M. Guo, W. Qi, F. Sun, A. Wang, Y. Guo, G. Zhu, J. Am. Chem. Soc. 133 (2011) 8778.
[60] X. Li, Y. Yan, Y. Lin, J. Jiao, D. Wang, D. Di, Y. Zhang, T. Jiang, Q. Zhao, S. Wang, J. Colloid Interface Sci. 494 (2017) 159.
[61] J. Yang, H. Su, W. Sun, J. Cai, S. Liu, Y. Chai, C. Zhang, Theranostics 8 (2018) 1966.
[62] L. Tong, Y. Zhao, T.B. Huff, M.N. Hansen, A. Wei, J.X. Cheng, Adv. Mater. 19 (2007) 3136.
[63] C.H. Hou, F.L. Lin, S.M. Hou, J.F. Liu, Int. J. Mol. Sci. 15 (2014) 17380.
[64] J.H. Doroshow, N. Engl. J. Med. 324 (1991) 843.
[65] H. Nohl, Biochem. Pharmacol. 37 (1988) 2633.
[66] C.M. Hessel, V.P. Pattani, M. Rasch, M.G. Panthani, B. Koo, J.W. Tunnell, B.A. Korgel, Nano Lett. 11 (2011) 2560.
[67] Q.L. Li, S.H. Xu, H. Zhou, X. Wang, B. Dong, H. Gao, J. Tang, Y.W. Yang, ACS Appl. Mater. Interfaces 7 (2015) 28656.